Earth and Planetary Science Letters 505 (2019) 76–85

Contents lists available at ScienceDirect

Earth and Planetary Science Letters

www.elsevier.com/locate/epsl

Relationships between grain size and organic carbon ^{14}C heterogeneity in continental margin sediments

Rui Bao [a,*], Thomas M. Blattmann [a], Cameron McIntyre [a,b,c], Meixun Zhao [d,e], Timothy I. Eglinton [a]

[a] Geological Institute, ETH Zurich, Zurich 8092, Switzerland
[b] Laboratory for Ion Beam Physics, Department of Physics, ETH Zurich, Zurich 8093, Switzerland
[c] Scottish Universities Environmental Research Centre, East Kilbride, G75 0QF, UK
[d] Key Laboratory of Marine Chemistry Theory and Technology (Ocean University of China), Ministry of Education, Qingdao 266071, China
[e] Laboratory for Marine Ecology and Environmental Science, Qingdao National Laboratory for Marine Science and Technology, Qingdao 266071, China

ARTICLE INFO

Article history:
Received 17 December 2017
Received in revised form 9 October 2018
Accepted 11 October 2018
Available online 25 October 2018
Editor: M. Frank

Keywords:
radiocarbon
^{14}C heterogeneity
grain size fractions
organic carbon
continental shelf sediments
hydrodynamic processes

ABSTRACT

The deposition and long-term burial of sedimentary organic matter (OM) on continental margins comprises a fundamental component of the global carbon cycle. A key unknown in interpretation of carbon isotope records of sedimentary OM is the extent to which OM accumulating in continental shelf and slope sediments is influenced by dispersal and redistribution processes. Here, we present results from an extensive survey of organic carbon (OC) characteristics of grain size fractions (ranging from <20 to 250 μm) retrieved from Chinese marginal sea surface sediments in order to assess the extent to which the abundance and isotope composition of OM in shallow shelf seas is influenced by hydrodynamic processes. Our findings show that contrasting relationships exist between ^{14}C contents of OC and grain size in surface sediments associated with two different hydrodynamic modes, suggesting that transport pathways and mechanisms imparted by the different hydrodynamic conditions exert a strong influence on ^{14}C contents of OM in continental shelf sediments. In deeper regions and erosional areas, we infer that bedload transport exerts the strongest influence on (decreases) OC ^{14}C contents of the coarser fraction, while resuspension processes induce OC ^{14}C depletion of intermediate grain size fractions in shallow inner-shelf settings. We use the inter-fraction spread in $\Delta^{14}C$ values, defined here as H^{14}, to argue that the hydrodynamic processes amplify overall ^{14}C heterogeneity within corresponding bulk sediment samples. The magnitude and footprint of this heterogeneity carries implications for our understanding of carbon cycling in shallow marginal seas.

1. Introduction

Investigations on the isotopic characteristics of organic matter (OM) in marine sediments provide important constraints on the functioning of carbon cycle, with radiocarbon (^{14}C) serving as a key tool for investigating carbon cycle processes in contemporary oceans. In addition to its value as a source indicator by virtue of the age of inputs materials, ^{14}C provides a window on the dynamics of carbon transfer between surface reservoirs on the Earth (Blair and Aller, 2012). Prior studies have demonstrated that ^{14}C contents of OM in marine surface sediments vary markedly, especially on continental margins (Griffith et al., 2010). This ^{14}C variability may reflect mixing of OM of different ages, and/or the impact of pre- and post-depositional sedimentation processes (Pearson and Eglinton, 2000; Griffith et al., 2010).

In many studies, including a recent investigation of the Chinese Marginal Seas (CMS; Bao et al., 2016), ^{14}C contents of organic carbon (OC) in bulk surface sediment are commonly measured to assess regional variations in OC ^{14}C characteristics. However, such bulk-level ^{14}C information renders it difficult to distinguish the influence of source variations versus dynamic processes on OM content and isotope composition. Several studies have shown that sub-fractions of bulk sediment (e.g., specific grain size or density fractions) may exhibit both different OC preservation characteristics, as well as its hydrodynamic properties, resulting in distinct carbon isotopic (incl. ^{14}C) signatures (Megens et al., 2002; Arnarson and Keil, 2007). The transport behavior of different grain size fractions is linked to hydrodynamic properties of different particles and the physical oceanographic regime of sedimentary envi-

* Corresponding author. Present address: Department of Earth and Planetary Sciences, Harvard University, Cambridge, MA, USA.
E-mail address: rui_bao@fas.harvard.edu (R. Bao).

https://doi.org/10.1016/j.epsl.2018.10.013

ronments (Thomsen and Gust, 2000; McCave and Hall, 2006). OM associated with different sedimentary grain-size fractions may thus be subject to different fates, particularly in continental shelf and slope settings that are characterized by strong, dynamic, and diverse hydrodynamic gradients. However, no studies have far investigated the intrinsic variability in OC ^{14}C contents among grain-size fractions within a broad spatial context that encompasses diverse hydrodynamic regimes, like marginal seas.

While marked spatial variability in bulk OC ^{14}C contents was previously found in the CMS surface sediments (Bao et al., 2016), corresponding variations of carbon isotopic composition (^{14}C and ^{13}C) of OM associated with specific grain size fractions were not examined in detail, hindering elucidation of underlying causes of this isotopic variability. A primary goal of this study is to examine spatial variations in carbon isotope characteristics, especially ^{14}C contents, among different grain size fractions of surface sediments from an extensive marginal sea system. We present a suite of measurements ($n = 163$) on the content (OC%), and carbon isotopic (^{14}C, ^{13}C) composition of OM associated with specific grain size fractions of surface sediments obtained from 34 locations in the CMS encompassing the Bohai Sea (BS), the Yellow Sea (YS), and the East China Sea (ECS) (Fig. 1). In addition to yielding new information on the controls on spatial variations of OC ^{14}C content, we discuss mechanisms of widespread ^{14}C heterogeneity to advance our understanding of carbon cycle processes in the CMS, and global continental margin systems.

2. Study area and samples

2.1. Hydrodynamic processes in the CMS

The CMS receives huge quantities of sediments primarily from the Yellow and Yangtze Rivers (Qiao et al., 2017). The sediments from the Yellow River are transported by seasonal currents and are mostly deposited in the BS and YS, whereas those from the Yangtze River are primarily delivered to the ECS, where they are strongly influenced by tidal energy and coastal currents (Zhu and Chang, 2000; Chen, 2009; Yang et al., 2011; Li et al., 2016). Hydrodynamic processes are responsible for the modern distribution pattern of surface sediments in the CMS (Zhu and Chang, 2000; Zhu et al., 2006; McKee et al., 2004; Shi and Wang, 2012; Zeng et al., 2015), and play a crucial role in the formation of mud-rich zones that are observed near river mouths, as mobile mud belts along the coasts, and as deposition centers in the YS (Milliman et al., 1985; Yang et al., 2011; Liu et al., 2006; Zeng et al., 2015; Li et al., 2016).

In the CMS, there are two main sediment transport modes affecting the distribution of sediments: The first mode is via resuspension processes that are fueled by current-driven mobilization and transport of finer-grained sediments which become entrained in continuous suspension-deposition loops. This mode of transport has been observed based on temporal observations and using relatively short-lived radionuclide tracers (e.g., ^{7}Be, ^{210}Pb, ^{234}Th) (Yang et al., 2011; Li et al., 2016; Wang et al., 2016a). The second mode involves bedload sediment transport under the stronger flow conditions, whereby coarser material moves in contact with the bed by sliding or rolling processes (Liu et al., 1998; Zhu and Chang, 2000; Harris and Wiberg, 2002). Depositional settings influenced by sediment resuspension include the coastal mud belts, deltaic mud patches, and the central YS depocenter (Liu et al., 2006; Wang et al., 2014; Zhou et al., 2015; Wang et al., 2016a). In contrast, the middle and outer shelf of the ECS is more strongly influenced by bedload transport (Sternberg et al., 1985; Keller and Yincan, 1985; Liu et al., 1998; Zhu and Chang, 2000; Gao and Collins, 2014), leading to a greater fraction of coarser particles in surface sediments (Zhu and Chang, 2000; Xing et al., 2012; Qiao et al., 2017). Overall, these two distinct hydrodynamic processes control the distribution and grain size characteristics of surface sediments on this broad and shallow continental shelf system (Milliman et al., 1985; Keller and Yincan, 1985).

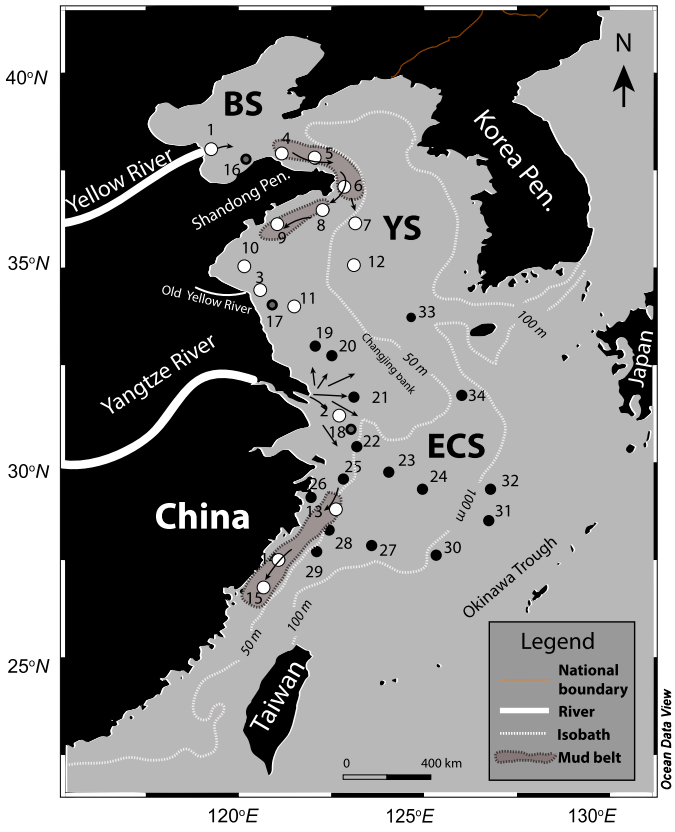

Fig. 1. Sampling locations of surface sediments in the CMS. Samples are categorized into hydrodynamic regime I (white solid symbols) and II (black solid symbols), respectively (see Table 1). Samples proximal to locations of fine-grained sediment accumulation in front of the river mouths (sample # 16, 17, 18) are shown as gray solid symbols. Regions outlined with dashed white lines depict the locations of coastal mud belts (Xu et al., 2009; Qiao et al., 2017). Arrows show the dominant sediment transport directions (modified from Chen, 2009).

2.2. Sampling from diverse hydrodynamic regimes

In this study, we selected a subset (34 samples) of the 358 surface (0–2 cm) CMS shelf sediment samples originally examined for bulk OC properties (Bao et al., 2016), and subjected them to more in-depth investigation. Based on the above-described hydrodynamic and sedimentological criteria, the selected samples can be overall classified into the two hydrodynamic regimes (regimes I and II, respectively, white and black symbols in Fig. 1, and Supplementary Fig. S1 for further information on selection criteria). One group of samples (Regime I) are located in the three river-mouth mud areas (sample #s 1, 2, 3) and the two coastal mud belts (samples #s 4, 5, 6, 8, 9, 13, 14, 15), that are characterized by strong resuspension on a seasonal basis (Li et al., 2016; Wang et al., 2016a) (Fig. 1). Since intense resuspension has also been observed in the western and central YS (Liu et al., 2006; Zhou et al., 2015), samples #s 7, 10, 11, 12 are also classified into Regime I. Most samples assigned to Regime I are from mud-rich areas (mean grain size: <63 μm, Table 1), and overlaps with the "Huanghe impact zone", "Changjiang impact zone" and "Inner ECS-YS shelf" regions as defined by van der Voort et al. (2018) using a clustering algorithm based on ^{14}C and total OC content. In contrast, samples mostly from deeper water (>50 m) of the ECS (sample #s 23, 24, 25, 27, 28, 29, 30, 31, 32, 33, 34) are generally character-

Table 1
The ^{14}C contents of organic matter among the different grain size fractions, and ^{14}C heterogeneity (H^{14}).

No.		Sample name	Location	Longitude (°E)	Latitude (°N)	Mean grain size (μm)[c]	Water depth (m)	$\Delta^{14}C$ (‰)						H^{14}
								<20 (μm)	20–32 (μm)	32–63 (μm)	63–125 (μm)	125–250 (μm)	Bulk[b]	
1	Regime I	B45	Deltaic mud area	119.00	38.32	16	21	−347.8 ±7.1[b]	−603.7 ±5.8[b]	−386.1 ±6.6[b]	−243.3 ±7.3		−362.9 ±6.5	360.4 ±13.1
2		P01		122.73	31.02	16	29	−302.9 ±6.9[b]	−408.8 ±6.7[b]	−428.7 ±6.2[b]	−509.9 ±5.2[b]		−305.3 ±7.2	207.0 ±12.1
3		H20		120.67	34.50	54	20	−433.2 ±6.3[b]	−638.3 ±4.3[b]	−776.8 ±3.5[b]	−768.3 ±2.5[b]	−545.4 ±4.6[b]	−499.9 ±4.3	343.6 ±9.8
4		B38	Mud belt of the Yellow Sea	121.16	37.91	31	22	−267.2 ±7.5	−418.1 ±6.7	−406.4 ±7.1	−357.6 ±6.9	−259.9 ±7.9	−231.2 ±3.8	158.2 ±14.6
5		B28		121.99	37.70	46	23	−217.5 ±9.3[b]	−415.9 ±6.3[b]	−314.0 ±7.3[b]	−346.9 ±7.0	−193.1 ±8.9	−246.8 ±8.1	222.8 ±15.2
6		B06		122.88	37.00	40	29	−308.6 ±7.6[b]	−343.7 ±7.6[b]	−342.0 ±7.9[b]	−332.1 ±7.1	−308.1 ±7.5	−283.7 ±8.0	35.6 ±15.1
7		B01		123.23	36.26	7	75	−196.0 ±7.8	−238.7 ±7.5	−203.6 ±7.6	−197.5 ±8.6	−202.1 ±7.7	−187.6 ±7.8	42.7 ±15.3
8		H01B		122.12	36.37	32	21	−264.0 ±7.9[b]	−439.3 ±6.8[b]	−355.6 ±7.7[b]	−381.4 ±7.2	−108.7 ±10.0	−256.0 ±9.4	330.6 ±16.8
9		H01		121.01	35.96	90	33	−244.3 ±8.2	−228.0 ±8.1	−217.9 ±8.5		−236.9 ±9.5	−174.6 ±4.1	26.4 ±16.7
10		H19	Resuspension area observed	120.34	35.00	42	28	−182.7 ±8.5	−268.6 ±7.8	−357.8 ±7.7	−341.5 ±8.3	−323.0 ±8.1	−209.0 ±7.7	175.1 ±16.2
11		H23		121.66	34.00	43	20	−397.9 ±7.8[b]	−663.2 ±5.8[b]	−708.6 ±4.9[b]	−697.8 ±3.7[b]	−575.8 ±6.6[b]	−447.3 ±4.0	310.7 ±12.7
12		C05		123.50	35.00	12	78	−254.2 ±8.5	−359.1 ±6.7[d]	−344.9 ±6.8	−390.2 ±7.6[d]	−165.3 ±8.2	−238.9 ±7.8	224.9 ±15.8
13		ME3	Mud belt of the East China Sea	122.58	28.73	12	63	−289.8 ±6.2[b]	−295.7 ±7.4[b]	−269.2 ±7.2[b]	−265.5 ±7.3	−283.5 ±7.5	−274.4 ±9.8	30.2 ±14.7
14		DH7-1		121.17	27.38	12	30	−287.8 ±7.7[b]	−442.8 ±5.6[b]	−383.9 ±8.9[b]			−289.3 ±7.1	155.0 ±13.3
15		DH8-1		120.83	26.77	13	47	−294.4 ±7.2[b]	−513.1 ±5.6[b]	−486.2 ±5.2[b]	−382.7 ±7.1		−318.6 ±7.2	218.7 ±12.8
16	Regime II	B70	Influenced by progradational processes[a]	120.12	37.72	29	17	−291.2 ±7.8[b]	−391.7 ±7.2[b]	−323.2 ±7.8[b]	−310.7 ±7.7	−659.2 ±5.1	−280.2 ±7.4	368.0 ±12.9
17		H21		121.00	34.00	17	19	−463.2 ±7.3[b]	−441.0 ±7.4[b]	−533.5 ±6.7[b]	−618.5 ±6.6[b]	−750.3 ±3.7[b]	−417.6 ±3.7	309.3 ±11.1
18		P02		123.01	30.84	229	47	−270.8 ±7.4[b,d]	−425.8 ±7.2[b,d]	−385.8 ±7.3[b,d]	−388.6 ±7.5[d]	−686.7 ±5.7[d]	−455.3 ±6.1	415.9 ±13.1
19		H36	Northern Part of the East China Sea strongly influenced by tide	122.00	33.00	171	14	−310.1 ±8.5	−487.7 ±7.5	−551.8 ±5.8	−775.9 ±3.5	−787.4 ±3.7	−677.7 ±5.1	477.3 ±12.2
20		R01		122.45	32.83	35	27	−235.7 ±7.3	−451.6 ±6.4	−391.1 ±6.8	−439.7 ±6.3	−402.9 ±8.6	−243.6 ±9.1	215.9 ±13.7
21		Z04		123.07	31.71	453	40	−120.7 ±8.6	−196.6 ±7.8	−307.3 ±6.6	−579.4 ±5.7	−685.3 ±4.5	−535.3 ±6.1	564.6 ±13.1
22		MZ13	Non-mud area of shallow part of the East China Sea	123.03	30.52	172	63	−222.8 ±8.4[b]	−311.6 ±6.6[b]	−296.2 ±7.0[b]	−490.2 ±5.9	−763.6 ±3.6	−340.0 ±6.8	540.8 ±12.0
23		P05		124.15	30.20	283	53	−176.4 ±8.9	−244.7 ±8.2	−207.8 ±7.7	−485.7±6.5	−624.3 ±7.7	−459.0 ±6.2	447.9 ±16.6
24		P07		124.95	29.90	239	56	−136.6 ±8.7	−176.5 ±8.8[d]	−424.4 ±6.1	−647.1 ±5.2[d]	−682.4 ±4.8	−377.2 ±6.0	545.8 ±13.5
25		DH4-0		122.88	29.52	39	54	−270.6 ±6.8[b]	−279.2 ±7.8[b]	−249.8 ±8.0[b]	−340.7 ±7.9	−490.8 ±7.2	−272.3 ±4.9	241.0 ±15.2
26		ME1		122.10	29.02	13	15	−321.9 ±7.4[b,d]	−421.9 ±6.7[b]	−443.2 ±6.5[b,d]	−567.8 ±5.6[d]		−346.9 ±6.8	245.9 ±13.0
27		ME5	Deeper part of the East China Sea	123.75	28.00	268	91	−257.2 ±8.9	−382.1 ±7.1	−439.7 ±6.8	−623.7 ±6.3	−693.4 ±5.1	−369.4 ±6.6	436.2 ±14.0
28		DH5-2		122.43	28.28	160	65	−309.4 ±7.2	−418.2 ±6.4	−427.0 ±6.9	−526.6 ±5.6	−823.7 ±3.5	−326.8 ±3.9	514.3 ±10.7
29		DH6-2		122.13	27.63	31	79	−314.4 ±7.9	−484.9 ±6.4	−575.6 ±6.2	−591.7 ±5.4	−517.5 ±6.3	−223.0 ±4.6	277.3 ±13.3
30		LS02		125.40	27.85	150	110	−135.0 ±8.3	−177.9 ±8.7	−316.7 ±7.6	−501.2 ±6.0	−421.0 ±6.2	−252.9 ±7.5	366.2 ±14.3
31		FP05		126.75	30.10	280	96	−182.9 ±7.2	−226.1 ±7.5	−193.0 ±7.7	−424.5 ±6.2	−549.9 ±5.8	−224.7 ±8.4	367.0 ±13.0
32		FP06		126.75	29.40	205	115	−160.8 ±8.6	−389.8 ±6.6	−424.9 ±7.3[d]	−584.1 ±6.3[d]	−574.5 ±5.2	−280.4 ±8.2	423.3 ±14.9
33		A07		124.83	33.79	302	81	−250.0 ±7.4	−246.5 ±7.4	−213.6 ±7.6	−217.8 ±7.7	−556.7 ±5.7	−302.8 ±7.5	343.1 ±13.3
34		F10		126.11	31.75	8	76	−259.6 ±7.9	−311.2 ±7.1[d]	−352.8 ±8.2[d]	−368.2 ±12.4	−568.2 ±5.9[d]	−272.9 ±7.7	308.6 ±13.8

Note: In general, with respect to Regime II, the lowest $\Delta^{14}C$ values occur in >63 μm fractions whereas the highest $\Delta^{14}C$ values occur in <63 fractions; and vice versa for Regime I. Due to distinct hydrodynamic condition for individual sampling location, it is reasonable that the minimum and maximum of $\Delta^{14}C$ values occur in different grain size fractions in Regime I and II.

[a] The samples (16, 17, 18) do not show an anomaly of $\Delta^{14}C$ distribution among grain size fractions compared with other samples in Regime II. Thus, their assignment to Regime II does not compromise the arguments based on Fig. 4B.

[b] Indicates that data is from Bao et al. (2016).

[c] Indicates that data is from Bao et al. (2016), except for sample H19. H19 was re-measured for grain size analysis in this study. The methodology was described in Tao et al. (2015).

[d] Indicates that the samples were graphitized using an automated graphitization system.

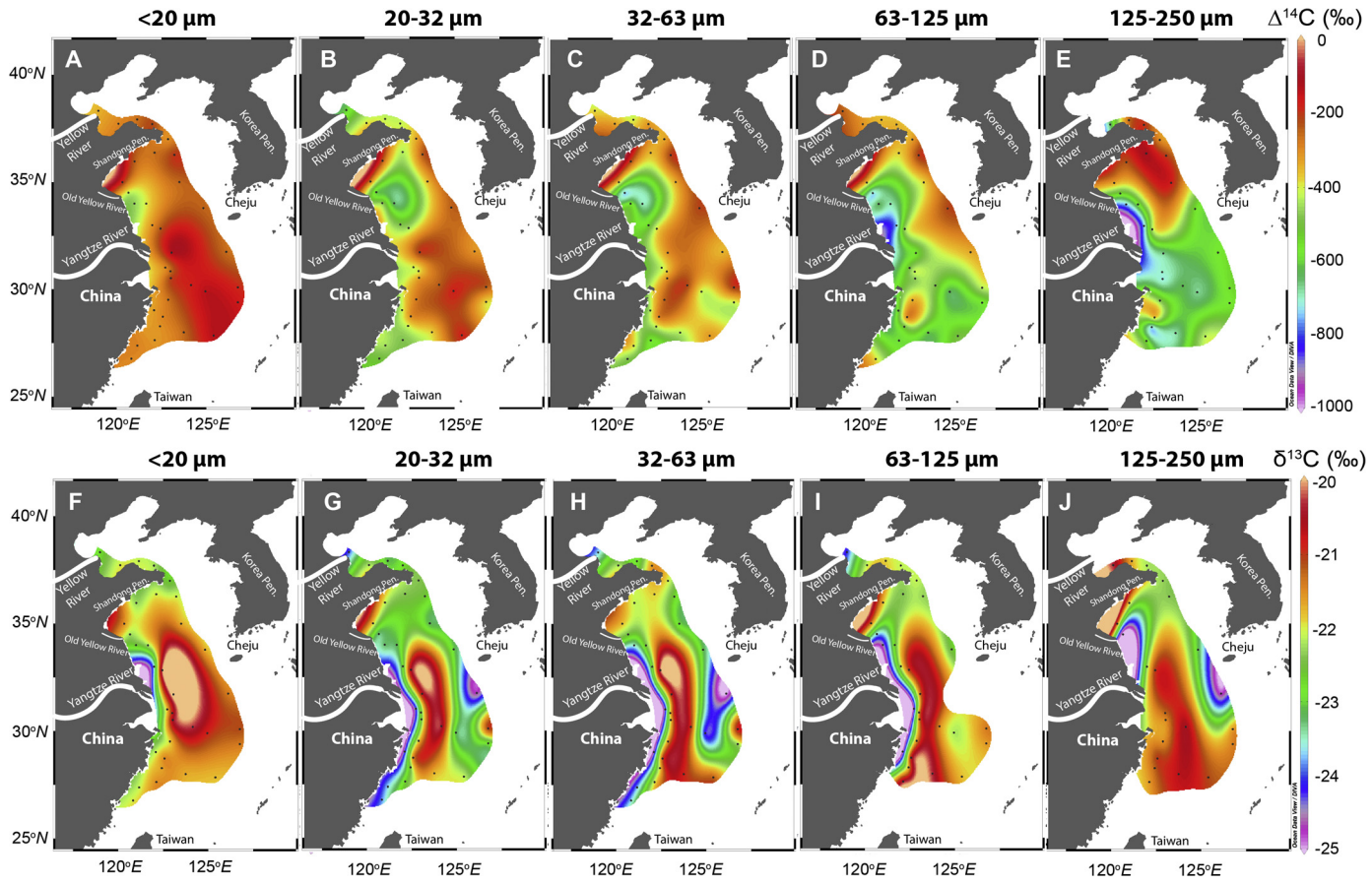

Fig. 2. Spatial variability (Ocean Data View Interpolation) of $\Delta^{14}C$ (A–E) and $\delta^{13}C$ (F–J) values of different grain size fractions of CMS surface sediments. Black dots are sampling locations (Table 1 and Supplementary Table 1). (For interpretation of the colors in the figure(s), the reader is referred to the web version of this article.)

ized by greater abundances of coarser material, assigned to Regime II (Table 1). The Changjiang bank area is a site of net erosion, with increased proportions of coarser sediments due to winnowing processes (Sternberg et al., 1985; Xing et al., 2012; Gao and Collins, 2014; Qiao et al., 2017), and thus samples from this region (sample #s 19, 20, 21) are also assigned to Regime II. We define a third class of depositional setting (sample #s 16, 17, 18; grey solid symbols, Fig. 1) – in locations proximal to the fine-grained sediments accumulating in front of the river mouths – that are interpreted to be influenced by progradational processes (Wang et al., 2014; Deng et al., 2017), and are provisionally assigned to Regime II. Regime II encompasses portions of the "Mid-ECS-YS shelf" and "Inner ECS-YS shelf" regions defined by van der Voort et al. (2018).

3. Methods

All samples were collected using a stainless steel box-corer and stored at −20 °C before analysis. The surface sediment samples were first freeze-dried and then wet sieved into <20, 20–32, 32–63, 63–125, and 125–250 μm fractions using stainless steel mesh sieves. Aliquots of freeze-dried grain size fractions were fumigated with HCl vapors to remove carbonates using a modified method of Komada et al. (2008). Briefly, after the dried samples were weighed into Ag capsules, they were placed on a ceramic tray above a beaker filled with 37% HCl that was placed at the bottom of a desiccator. The desiccator was evacuated and the samples were heated in an oven at 60 °C for 72 h. After fumigation, excess acid was neutralized by replacement with ~20 g NaOH pellets in a pre-combusted Petri dish (60 °C for 72 h). The fumigated samples were measured for OC % and stable organic carbon isotopic compositions ($\delta^{13}C$, ‰VPDB) using an Elementar Vario MICROcube elemental analyzer coupled to an Isoprime VISION isotope ratio mass spectrometer calibrated against standard materials at ETH Zurich. Corresponding $\delta^{13}C$ values were determined to an accuracy of better than ± 0.1‰ and OC % to better than 0.03% based on standards. The fumigated samples (~100 μg carbon for each sample) were either prepared via sealed tube combustion and analyzed directly as CO_2 gas (Ruff et al., 2007) or, in the case of some larger samples (~500 μg C, cf. Table 1), were graphitized using an automated graphitization system (Wacker et al., 2010) for ^{14}C measurements. All gas and graphite samples were analyzed for ^{14}C using a MIni CArbon DAting System (MICADAS) at the Laboratory for Ion Beam Physics, ETH Zurich (Synal et al., 2007). ^{14}C data are reported as $\Delta^{14}C$ values (‰).

4. Results

We report values for OC %, ^{13}C, and ^{14}C isotopic compositions of the CMS sediment samples (^{14}C data includes 108 new measurements and published data ($n = 55$): Fig. 2A–E and Table 1; ^{13}C data: Fig. 2 F–J and Supplementary Table S1; OC % data: Supplementary Table S2). The <20 μm fractions exhibit OC contents ranging from 2.71 to 0.46% (ave. 0.95 ± 0.48 (1σ)%, $n = 34$), $\delta^{13}C$ values ranging from −23.9 to −19.7‰ (ave. −21.7 ± 0.8 (1σ)%, $n = 34$), and $\Delta^{14}C$ values ranging from −463.2 to −120.7‰ (ave., −263.4 ± 79.2 (1σ)‰, $n = 34$). The 20–32 μm fractions exhibit a larger range of OC contents (1.73 to 0.09%; ave. 0.54 ± 0.38 (1σ)%, $n = 34$), $\delta^{13}C$ values (−24.8 to −20.3‰; ave. −22.6 ± 1.1 (1σ)%, $n = 34$), and $\Delta^{14}C$ values (−663.2 to −136.6‰; ave., −374.7 ± 125.7 (1σ)‰, $n = 34$). The 32–63 μm fractions exhibit OC contents ranging from 1.18 to 0.07% (ave. 0.38 ± 0.30 (1σ)%, $n = 34$), $\delta^{13}C$ values ranging from −25.1 to −20.1‰ (ave. −22.4 ± 1.2 (1σ)%,

$n = 34$), and $\Delta^{14}C$ values ranging from −776.8 to −193.0‰, (ave., −383.3 ± 134.0 (1σ)‰, $n = 34$). The $\Delta^{14}C$ values of 63–125 and 125–250 μm fractions exhibit a relatively large range of −775.9 to −197.5‰, (ave., −458.4 ± 155.2 (1σ)‰, $n = 32$) and −823.7‰ to −108.3‰, (ave., −481.7 ± 224.6 (1σ)‰, $n = 30$), respectively (Fig. 2); corresponding $\delta^{13}C$ values of 63–125 and 125-250 μm fractions range from −25.5 to −20.3‰ (ave. −21.7 ± 1.2 (1σ)%, $n = 30$) and −25.0 to −20.3‰ (ave. −22.1 ± 1.2 (1σ)%, $n = 30$) respectively; the OC contents of 63–125 and 125–250 μm fractions are ranging from 1.51 to 0.06% (ave., 0.31 ± 0.31 (1σ)%, $n = 30$) and 1.60 to <0.01% (ave., 0.50 ± 0.42 (1σ)%, $n = 24$), respectively.

5. Discussion

5.1. Patterns of spatial variability in OM $\Delta^{14}C$ among grain size fractions

There are marked differences in the spatial variation of ^{14}C contents for the different grain size fractions (Fig. 2 A–E). For the finer fractions (<20, 20–32, and 32–63 μm), the $\Delta^{14}C$ values of more distal sediments in the YS (e.g., sample #s 7 in the center of the YS) are generally higher (i.e., younger ^{14}C ages) than those on the inner shelf of northern Shandong Peninsula (e.g., sample #s 1, 4, 5) (Fig. 2A–C). Lower $\Delta^{14}C$ values (older ^{14}C ages) of the latter could be partly explained by fluvial supply of pre-aged OC from the Yellow River ($\Delta^{14}C$ values of Yellow River suspended particulate OM (POM): ∼ −400‰, Wang et al., 2012; Tao et al., 2015). However, despite of large-scale export (∼30%, Yang and Liu, 2007) of Yellow River-derived sediments to the central YS, OM in the central YS exhibits less depleted $\Delta^{14}C$ values. While the central YS and coastal area along the northern Shandong Peninsula are both influenced by fluvially-derived terrestrial OC, there is significantly higher marine primary productivity in the latter than in the former (Shi and Wang, 2012). Marine OM with higher $\Delta^{14}C$ values (reflecting those of dissolved inorganic carbon, DIC: ∼−25 to −160‰, in the BS; Wang et al., 2016b) should thus compensate for inputs of ^{14}C-depleted terrestrial OM in sediments to these shallow near-shore settings. However, we find relatively low $\Delta^{14}C$ values for OM accumulating along the northern Shandong Peninsula, indicating that ^{14}C contents cannot be solely explained by a mix of allochthonous and autochthonous carbon sources. Overall, these observations reveal marked spatial variability in $\Delta^{14}C$ values in the BS and YS that cannot readily be explained based solely on OC inputs.

Higher $\Delta^{14}C$ values are also exhibited by the finer grain size fractions (<20, 20–32, and 32–63 μm) on the outer shelf of the ECS (e.g., sample #s 21, 23) than those in the coastal area (e.g., sample #s 14, 15) (Fig. 2A–C). Similarly, the $\delta^{13}C$ values of these fractions in deeper shelf settings are also higher than those in the nearshore zone (Fig. 2F–H). While ^{13}C depletion in the latter can be interpreted as a result of inputs of Yangtze River POM, the relatively low $\Delta^{14}C$ values are not consistent with that of OC associated with fluvially exported SPM ($\Delta^{14}C$ ∼−110‰, Wang et al., 2012). It is difficult to reconcile these observations only by carbon end-member mixing. In addition, given that sedimentation rates along the coastal mud belt of the ECS (>1.5 cm/yr, Liu et al., 2006; Qiao et al., 2017) are higher than on the middle/outer shelf, and that the sediment mixed layer depths (i.e., ∼10 cm; Su and Huh, 2002; Liu et al., 2006) are significantly greater than that of the sampling interval (0-2 cm), bioturbation processes are unlikely to account for older OC observed in the finer grain-size fractions of surficial sediments from these shallow regimes (Griffith et al., 2010). Instead, the carbon isotopic variability of OM residing in finer-grained fractions may reflect a combination of different OC sources as well as resuspension-related processes occurring on the shallow inner shelf that induce OM "pre-aging" and associated transformations (Bao et al., 2016).

The aforementioned lines of evidence suggest that hydrodynamic processes in deeper regions of the CMS differ from those in shallow areas, and these differences may influence the fate of OM associated with fine-grained sediments. One potential explanation for higher $\Delta^{14}C$ values on the outer shelf is vertical particle export associated with biological pump processes, which varies seasonally (Chen, 2009; Fu et al., 2015; Wu et al., 2016), while fine-grained sediments are prone to erosion and ocean-ward export (Zhu and Chang, 2000; Zhu et al., 2006; Gao and Collins, 2014). Alternatively, rapid lateral advection of ^{14}C-enriched and ^{13}C-depleted OM from deltaic environments to deeper regions may occur via surface current-driven transport (Yang et al., 2007), contributing to the elevated $\Delta^{14}C$ values of finer grain size fractions in the deeper part of the ECS (e.g., sample #s 34, southern Cheju island). These contrasting hydrodynamic regimes of shallow (inner) and deeper (outer) shelf environments may thus contribute to the observed spatial variability in ^{14}C contents of OM in finer-grained sediment phases.

Coarser grain size fractions (63–125 and 125–250 μm) exhibit markedly different spatial variations in $\Delta^{14}C$ values compared with the corresponding finer (<63 μm) fractions (Fig. 2D, E). The $\Delta^{14}C$ values of coarser fractions in the western YS are very low (<−600‰). These low $\Delta^{14}C$ values could reflect preferential loss of labile (younger) OC due to erosional processes and to continued oxygen exposure in these "incineration" regions (Aller and Blair, 2006; Mollenhauer and Eglinton, 2007) that leave a residual pool of older OC. In the northern and central YS and BS, for example, coarser fraction $\Delta^{14}C$ values are generally higher than those in the ECS. Rapid sedimentation in the former settings may result in higher $\Delta^{14}C$ values (Qiao et al., 2017). In deeper regions of the ECS, the combination of bioturbation processes and relatively low sedimentation rates (∼1 mm/yr, Qiao et al., 2017) might contribute to the presence of ^{14}C-depleted OC in coarser sediment fractions. Nevertheless, these processes are insufficient to explain the large (∼500‰) $\Delta^{14}C$ offset between corresponding grain size fractions from the northern and central YS/BS and from the middle shelf of the ECS. We also note that coarser fractions from the middle shelf of the ECS that exhibit low $\Delta^{14}C$ values (Fig. 2D, E) are generally enriched in ^{13}C (Fig. 2I, J), suggesting that ^{14}C depletion in coarser-grained mid- and outer-shelf sediments may not simply reflect degradation of younger and fresher (marine) OM under slower sedimentation conditions.

5.2. Carbon isotopic relationships among grain size fractions

We evaluate OM compositional relationships among grain size fractions in order to shed further light on underlying processes. Relationships between ^{14}C, ^{13}C, and OC% for Regime I (white solid symbols) and II (black solid symbols) are shown in Fig. 3. For the finer fractions (<63 μm), Regime I and II samples show similar relationships (patterns) between $\Delta^{14}C$ and OC% values, whereas corresponding coarser fractions (e.g., 125–250 μm) exhibit contrasting relationships between the two Regimes (Fig. 3A). Coarser fractions from Regime II display a wider range of $\Delta^{14}C$ values (∼−800 to −400‰) but exhibit a narrower range of OC% contents compared with Regime I. These characteristics may imply different controls on $\Delta^{14}C$ values of coarser fractions in the two Regimes. While degradation of more labile (younger) OC from coarser fractions due to limited surface area protection could explain greater ^{14}C depletion for these fractions from Regime II (Fig. 3A iv, v), they exhibit a relatively broad range of $\delta^{13}C$ values (∼−25 to −20‰, Fig. 3B), suggesting that the selective degradation processes are unlikely to be the only cause for the pattern in $\Delta^{14}C$ values (cf., Goñi et al., 2005).

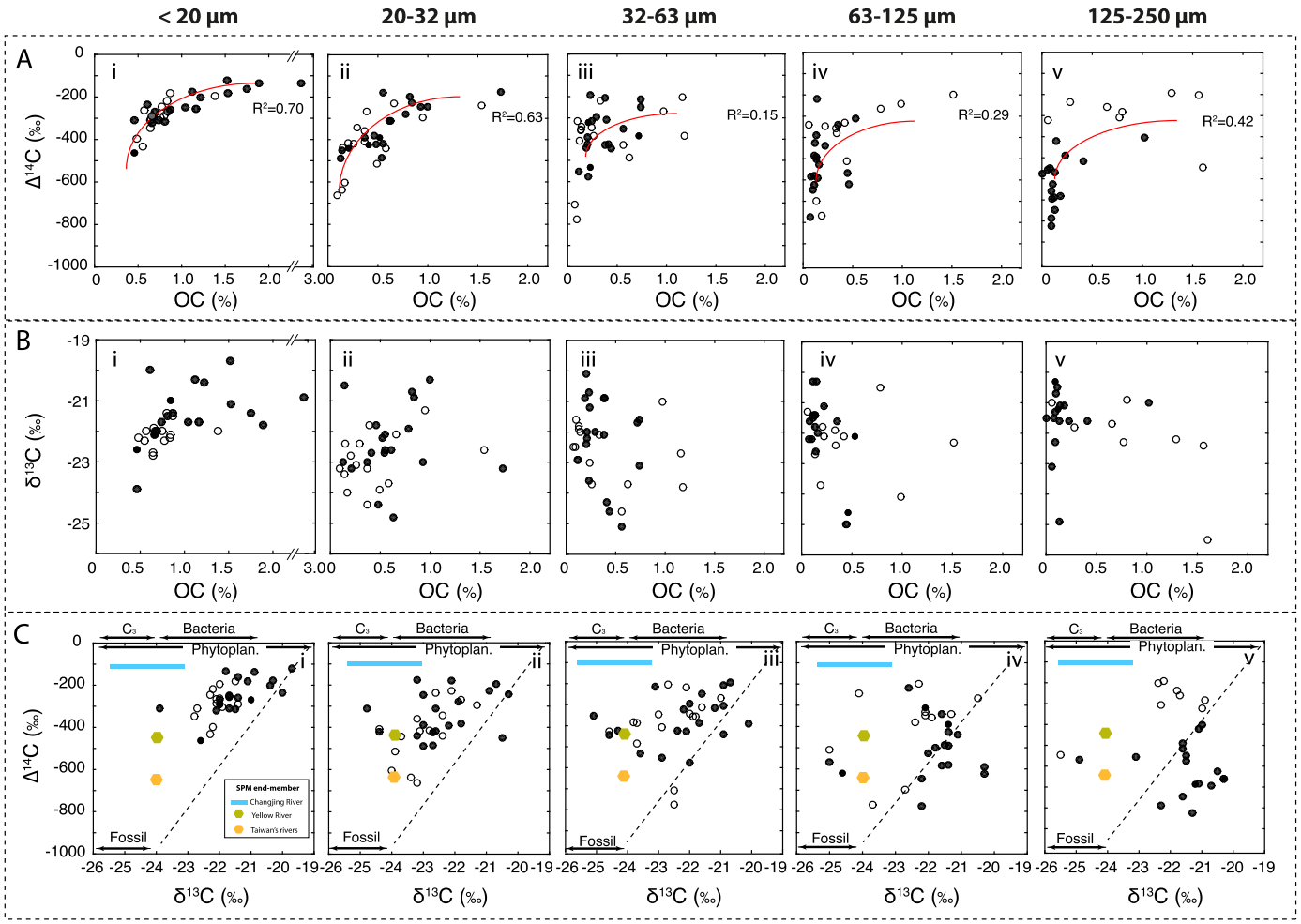

Fig. 3. Matrix of cross-plots between: (A) $\Delta^{14}C$ and OC %, (B) $\delta^{13}C$ and OC %, and (C) $\Delta^{14}C$ and $\delta^{13}C$ for different grain size fractions from Regime I (white solid symbols) and Regime II (black solid symbols) (<20 μm (i), 20–32 μm (ii), 32–63 μm (iii), 63–125 μm (iv), and 125–250 μm (v)). The OC source end-members and dashed lines are taken from Goñi et al. (2005) and references therein. Samples with $\Delta^{14}C$ and $\delta^{13}C$ values to the left of the line may be explained by mixing of different OM end-members. The $\Delta^{14}C$ and $\delta^{13}C$ end-members of SPM in the regional rivers derive from Tao et al. (2015, Yellow River), Wang et al. (2012, Yangtze River), and Kao et al. (2014, Taiwan rivers).

A plot of ^{13}C versus ^{14}C values is frequently utilized to assess the OC source characteristics and aid in assignment of isotopic end-members. Our results show that the $\delta^{13}C$ and $\Delta^{14}C$ values of the majority of finer fraction samples (i.e., <20, 20–32, and 32–63 μm) may be explained by mixing of different OM end-members derived from allochthonous (modern, pre-aged and fossil terrestrial OM derived from riverine SPM) and autochthonous (marine productivity) sources (Fig. 3C i–iii). However, additional processes may contribute to the scatter in this parameter space. In particular, preferential remineralization of recently-synthesized biogenic materials relative to allochthonous pre-aged terrigenous and marine organic components during the transport and sedimentation processes would result in depletion in ^{14}C and ^{13}C (Mollenhauer and Eglinton, 2007; Bao et al., 2016). Moreover, transport-related OM aging associated with hydrodynamic processes (e.g., entrainment in resuspension-deposition loops) on the inner shelf would also result in a downward shift in the plot (Bao et al., 2016). The effects of the above aforementioned processes (e.g., preferential remineralization of OM, impact of hydrodynamics on OM) are difficult to determine in these classic isotopic plots.

In contrast to their finer-grained counterparts, coarser fractions (63–125, 125–250 μm) from Regime II generally plot on the right side of dashed line (Fig. 3C iv, v), whereas those from Regime I tend to plot on the left of the line. Relative enrichment of fossil or pre-aged terrestrial OC in coarser detrital sediment grains could explain the lower $\Delta^{14}C$ values for the coarser fractions in Regime II, however terrestrial materials discharged by the major rivers surrounding the CMS (both from mainland China and Taiwan) are generally fine-grained (mean grain size: <63 μm, Tao et al., 2015; Hilton et al., 2010) and depleted in ^{13}C ($\delta^{13}C$ in Yangtze River: ∼−26 to −23‰; Yellow River: ∼−24‰, Wang et al., 2012; Tao et al., 2015; Taiwan small rivers: ∼−24‰, Kao et al., 2014; Hilton et al., 2010) compared to those of coarser grains size fractions from Regime II (ave. −21.8‰). There is no strong evidence for transport of coarse-grained sediments to the regions of the ECS investigated in this study (Fig. 2E). In addition, bedload transport only accounts for small percentage (<1%) of the exported fluvial sediment (i.e., Yangtze River, Yang et al., 2015), and is thus unlikely to contribute significantly to coarser (>63 μm) fractions of distal shelf sediments (e.g., sample# 24, >90% mass percentage in bulk sample, Supplementary Table S3). Moreover, Liu et al. (2008) demonstrated that terrigenous materials exported by Taiwanese rivers is transported either northeastward into the Southern Okinawa Trough or southward into the South China Sea, rather than middle shelf of the ECS (van der Voort et al., 2018). The above observations thus suggest that other factors, besides the sources, control the carbon isotopic composition (esp. ^{14}C contents) of coarser fractions in Regime II compared with corresponding fractions in Regime I.

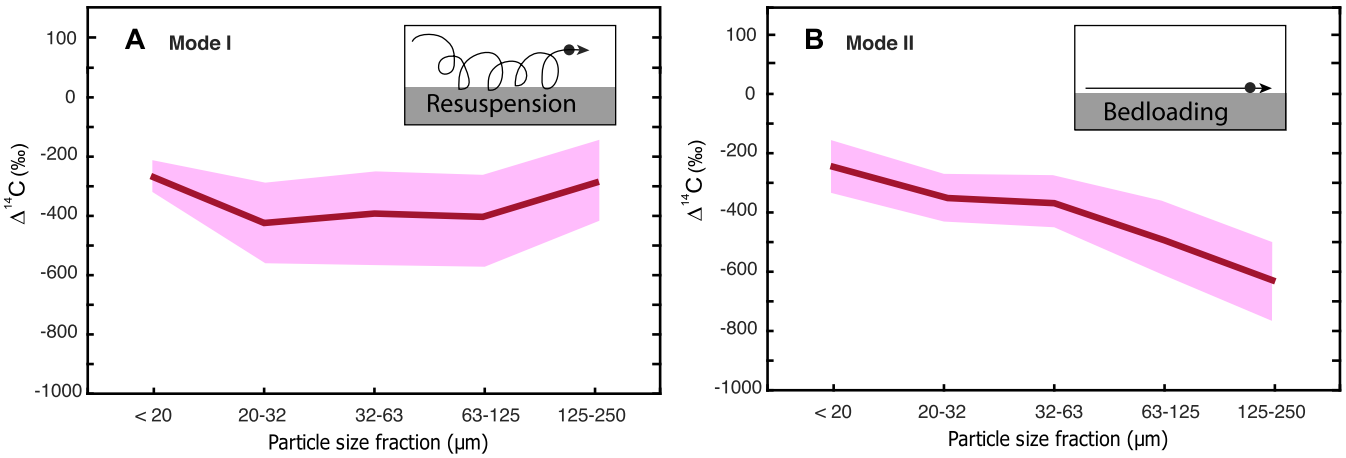

Fig. 4. Relationship between $\Delta^{14}C$ values and grain size: (A) "U"-shaped pattern of $\Delta^{14}C$ values (Mode I); the red line corresponds to the average $\Delta^{14}C$ value for each fraction $\Delta^{14}C$ values; the magenta envelope shows the error (1σ; $n = 15$). There is a statistically significant difference (ANOVA, $p < 0.05$) among the $\Delta^{14}C$ values of grain size fractions. (B) Quasi-linear trend of decreasing $\Delta^{14}C$ values with increasing grain size (Mode II) (1σ; $n = 19$). The schematic inserts show the main hydrodynamic processes at work in the respective regimes – (I) resuspension; (II) bedload transport.

5.3. Differential hydrodynamic influences on ^{14}C contents

Generalized relationships existing between ^{14}C contents of OC and grain size in surface sediments are shown in Fig. 4. We attribute the contrasting trends between regimes to differing influences of underlying hydrodynamic processes. Specifically, based on the distinctive OC characteristics of specific grain size fractions of the representative sedimentation locations from Regime I and II, we suggest that (at least) two different hydrodynamic modes influence ^{14}C contents of CMS surface sediments:

In the first mode, as exemplified by Regime I, minimum $\Delta^{14}C$ values are associated with intermediate grain sizes (Fig. 4A). This includes the "sortable silt" (20–63 μm) component that requires lower shear stress to be eroded and returned to suspension (McCave and Hall, 2006), through which associated OM may experience prolonged oxygen exposure and transport times that in turn promote greater lateral redistribution, degradation and aging of OM relative to that residing in other grain size fractions (Bao et al., 2016). Such ^{14}C age-grain size relationships are likely to be prominent in regions where prevailing and seasonally oscillating coastal currents transport and disperse entrained sediment in shallow water environments. The grain size fraction with minimum $\Delta^{14}C$ value likely depends on local shear stress (Zhu and Chang, 2000), but mostly manifests itself in the finer fractions (<63 μm, Table 1). Aggregation/disaggregation processes occurring in the sedimentary matrix, which are prevalent in shallow regions (Wang et al., 2015), may also impact $\Delta^{14}C$ values of OM, particularly that associated with intermediate grain size sediments. Such aggregation/disaggregation processes may occur during deposition-resuspension cycles (Thomsen and Van Weering, 1998) and lead to relatively "uniform" ^{14}C contents among the intermediate (20–32, 32–63, and even 63–125 μm) grain size fractions compared with those in the finer and coarser fractions (Fig. 4A).

In contrast to the "U-shaped" pattern for Regime I, the mode that characterizes Regime II is associated with a quasi-linear decrease in $\Delta^{14}C$ values from fine to coarse fractions (Fig. 4B; Table 1). Finer particles in sediments from Regime II are presumed to be less susceptible to resuspension and therefore less prone to incineration processes operative in energetic coastal settings (Aller and Blair, 2006; Yang et al., 2007). In deeper waters of the outer shelf, finer-grained sediments may also be exported to the abyssal ocean, potentially via nepheloid layer transport (Zhu et al., 2006; Gao and Collins, 2014), resulting in preferential accumulation of coarser sediments in the deeper part of ECS (Supplementary Table 3), while finer-grained sediments deposited in the vicinity of river mouths (also included in Regime II) are also eroded by progradational processes (McKee et al., 2004).

In contrast, coarser-grained sediments are less prone to rapid seaward export under the prevailing hydrodynamic conditions. Instead, sluggish bedload movement serves as the prevailing transport mechanism (Zhu and Chang, 2000; Sternberg et al., 1985; Keller and Yincan, 1985; Liu et al., 1998; Gao and Collins, 2014), leading to pronounced ^{14}C aging (via radioactive decay) of residual OM within the coarser grain size fractions. We argue that sluggish across-shelf lateral movement via bedload transport, accompanied by selective degradation OC of coarser fractions, induces the apparent ^{14}C aging. Due to relatively low surface ocean productivity on the mid-shelf of the ECS (Shi and Wang, 2012), influence of dilution by hemipelagic sedimentation on our interpretation would be minimal. During transport, such bedload materials may entrain OM derived from marine benthic production in the shallow regions (Thomsen and Gust, 2000; Jahnke et al., 2000), contributing to higher $\delta^{13}C$ values (France, 1995) for OM associated with coarser sediments in Regime II.

Arnarson and Keil (2007) found that encapsulation within biomineral matrices was the dominant mode of OM association with sedimentary particles exposed to relatively long oxygen exposure times (OET, i.e., >1000 yr), and these authors speculated that the associated OC may include residual marine material previously residing in organic–mineral aggregates. Mineral protection may develop with protracted lateral transport (i.e., long OET) (Arnarson and Keil, 2007), potentially resulting in accumulation of recalcitrant OC in coarser fractions (Bao et al., 2018). Such an interpretation is consistent with the older OC ^{14}C ages of coarser-grained sediments exposed to prolonged OET, and this – together with more sluggish bedload transport – would explain the observed trend of decreasing $\Delta^{14}C$ values with increasing grain size.

Variations in (bio)diffusion coefficients as a function of grain size may lead to different residence times in the sediment mixed layer, with coarser particles generally exhibiting longer residence times (Thomson et al., 1995). While this may also partially explain the observed trend (Fig. 4B), such processes are unlikely to account for the large offset of $\Delta^{14}C$ values observed between finer and coarser fractions (max. ~600‰, ~5000–7000 ^{14}C yr) given the relatively small differences in residence times of particles of different sizes in the mixed layer of continental shelf sediments (Thomson et al., 1995). Bröder et al. (2018) determined a lateral transport time of OC of ~3600 years across the ~600 km-wide Laptev Sea shelf. In our case, given a very similar transport distance from the coast to the outer shelf of the ECS, millennial-scale lateral

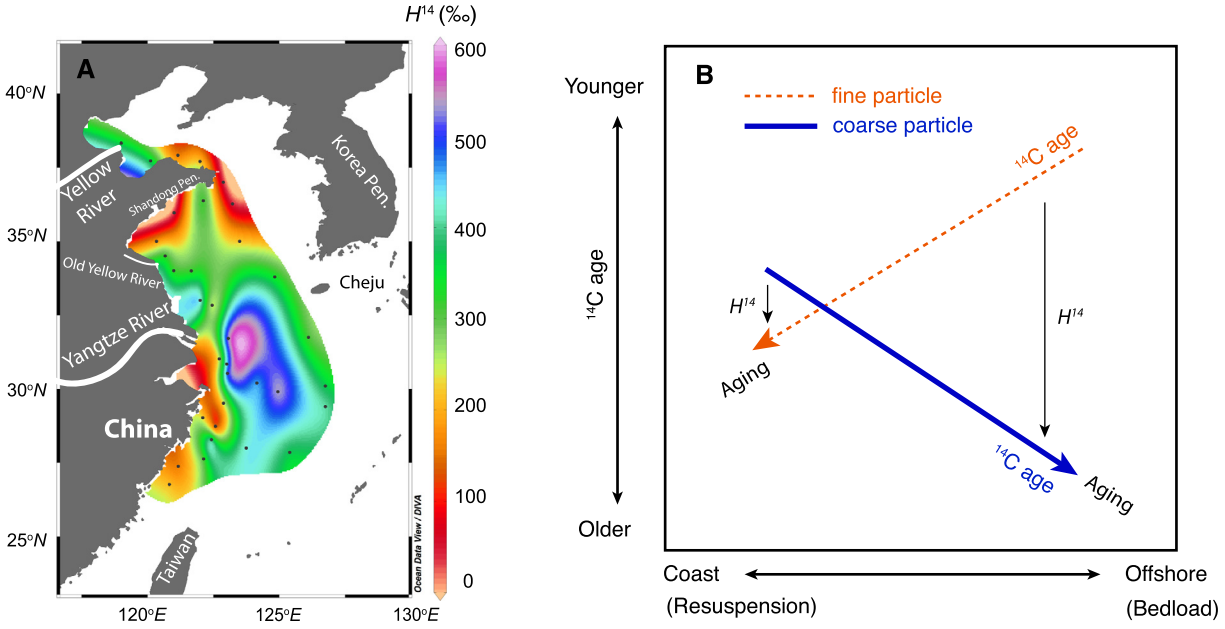

Fig. 5. (A) Spatial variability in H^{14} (^{14}C heterogeneity) in the CMS. (B) A conceptual model indicates changing H^{14} from coast to offshore. The red line exemplifies the evolution of finer grain size fraction ^{14}C ages; the blue line indicates the evolution of coarser grain size fraction ^{14}C ages. The difference in Δ^{14}C values between the two lines, the arrows represent the magnitude of H^{14}.

transport times for OM associated with coarser sediments seems reasonable (assuming that lateral transport time can be roughly calculated through offsets of OC ages observed between finer and coarser fractions).

Irrespective of the specific processes responsible for the large Δ^{14}C offset between the finest and coarsest fraction, the processes are each in some way linked to hydrodynamic effects that exert different influence as a function of sediment grain-size. Consequently, we conclude that contrasting transport pathways and mechanisms imparted by different hydrodynamic regimes are largely responsible for observed contrast in grain size-vs–^{14}C patterns (Fig. 4). Hydrodynamic processes thus appear to play a critical role in dictating the heterogeneity in ^{14}C among different sedimentary grain size fractions of CMS surface sediments.

5.4. Assessing intrinsic ^{14}C heterogeneity in OM

Building on the above premise, the heterogeneity in Δ^{14}C values of OM associated with different grain size fractions carries information on hydrodynamic influences on the dispersal and burial of OM in marginal sea sediments. Taking Fig. 4B as an example, and assuming that there is a continuum of sedimentary grain sizes comprising bulk sediments (Supplemental Figure S2B), then it is reasonable to assume a spectrum of ^{14}C contents of OM exists as function of grain size. If we extrapolate to extremely large (i.e., immobile) grain sizes, then Δ^{14}C values should approach −1000‰, implying that differences between fine and coarse-grained fractions would reach a maximum. To a first approximation, the magnitude of this ^{14}C "heterogeneity", defined as the difference in OM ^{14}C contents between sedimentary grain size fractions, should thus reflect the degree of influence imparted by hydrodynamic processes. The ^{14}C offset between the highest and lowest Δ^{14}C values within a grain size spectrum, here termed "H^{14}", may be applicable for other regimes that are under hydrodynamic influence, and serve as a semi-quantitative metric of ^{14}C heterogeneity within sedimentary OM (Table 1).

The spatial variation in H^{14} values for CMS sediments is shown in Fig. 5A. H^{14} values are relatively small (190 ± 14 (1σ)‰), i.e., indicating low heterogeneity, in regions where sediment resuspension processes exert a strong influence on sediment mobilization and deposition (Regime I – the YS and ECS coastal mud belts and in the central YS), whereas H^{14} values are higher (390 ± 13 (1σ)‰) in Regime II. For the former, all grains size fractions are subject to resuspension, albeit to different extents, leading to smaller discrepancies among Δ^{14}C values (i.e., lower H^{14} values). On the other hand, in Regime II, sluggish bedload movement of coarser-grained fractions via tidal and bottom currents (Zhu and Chang, 2000; Zhu et al., 2006), coupled with more rapid and ephemeral vertical and lateral export/supply of younger, OM associated fine-grained sediments result in amplified ^{14}C heterogeneity (higher H^{14} values).

Numerous studies have sought to understand changes in carbon biogeochemistry along across-shelf transects in the CMS (Fig. 5A, Tsunogai et al., 1999; Zhu et al., 2006). Building on our findings, the measured ^{14}C ages of OM associated with the finest and coarsest sediment fractions may be envisioned to exhibit a "scissor-like" pattern (Fig. 5B) whereby the different aforementioned hydrodynamic processes result in a general increase in ^{14}C heterogeneity (H^{14}) from relatively shallower to deeper shelf regions. This simple conceptual model may serve as a framework for understanding processes influencing sedimentary OM in marginal sea systems. The influence of hydrodynamic processes in the fate of OC would be expected to vary substantially based on continental margin setting. Intermediate and bottom nepheloid layer transport of OC hosted on fine-grained particles (Inthorn et al., 2006), and bedload transport of OM associated with coarser grain size fractions serve as vectors for export of OC to distal environments (Fig. 6). Together, these two "conveyers" move OC across the shelf with different efficiencies and over different timescales. The "continental shelf pump" was first proposed to describe the absorption and export of CO_2 in shelf waters (Tsunogai et al., 1999). This concept can be extended to also account for lateral transport of particulate OC (POC) (Fig. 6). Hydrodynamic processes (e.g., resuspension, bedload transport) may enhance remineralization of OM, in turn influencing dissolved organic and inorganic carbon fluxes.

Given that resuspension-driven and bedload transport exert different influences on the dynamics, the differential transport behavior may manifest in changes of the ^{14}C content of sedimentary OM. It is reasonable, therefore, to assume that differences in ^{14}C con-

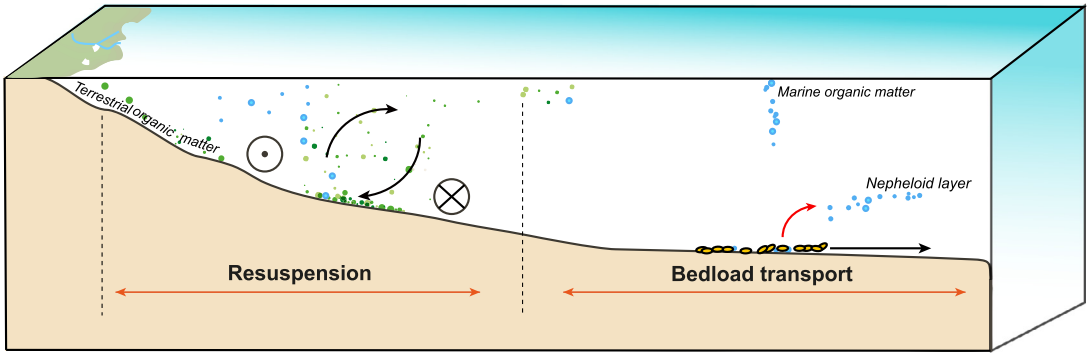

Fig. 6. Conceptual model showing the "continental shelf pump" of POC highlighted through two transport modes: resuspension and bedload transport.

tents between grain size fractions due to hydrodynamic processes may be represented by the H^{14} proxy. This H^{14} implication would provide the estimation of the influences of hydrodynamic processes (resuspension) in the ^{14}C contents in the shallow marginal seas, where other approaches (e.g., sediment ^{230}Thxs inventories) may not allow useful approximations of resuspension (Mollenhauer et al., 2011). The concept may be applicable to other settings given that hydrodynamic processes can affect grain size distributions of deep-ocean sediments (McCave and Hall, 2006). Building on the observed $\Delta^{14}C$-grain size relationship in Regime II, our conceptual model suggests that $\Delta^{14}C$ values will decrease with increasing grain size (i.e., high H^{14} values) of detrital sediments in deep-sea environments. Indeed, Bao et al. (2018) found that ^{14}C ages OM systematically increased from the finest (<20 μm) to the coarsest fraction (>500 μm) (equivalent to H^{14}: ~300‰) in a deep-sea sediment sample from the Arabian Sea (~ 4000 m water depth). In most cases, high H^{14} values indicate pronounced bedload transport, whereas low H^{14} values are characteristic for re-suspension. However, in highly energetic and shallow margins, where hydrodynamic processes may result in mobilization of both finer and coarser sediments to the suspended load (e.g., tidally-influenced regions of the northwestern ECS, Xing et al., 2012), OC aging in both fractions may occur, potentially leading to a "crossing point" in Fig. 5B. Under these conditions, H^{14} would not detect or underestimate the influence of hydrodynamic processes as expressed by ^{14}C contents, highlighting a limitation of the approach. Nevertheless, markedly lower $\Delta^{14}C$ values of all grain size fractions are often observed in these settings, providing an additional line of evidence to infer hydrodynamic influence on sedimentary OC.

6. Conclusions and implications

In this study, we present an extensive survey of ^{14}C, ^{13}C and OC contents of OM associated with different grain size fractions of surface sediments from the CMS. Our results reveal both strong spatial variability in ^{14}C contents of specific grain size fractions as well as distinctive ^{14}C patterns among grain size fractions from specific samples. These variations in the relationship between sediment grain size and OC ^{14}C content are linked to the underlying hydrodynamic processes. We propose that two different transport modes (resuspension-driven and bedload transport) contribute to the patterns and magnitude of heterogeneity in ^{14}C among grain size fractions, the latter defined here as "H^{14}" – the offset between maximum and minimum $\Delta^{14}C$ values. In deeper waters, sluggish bedload transport of coarser-grained sediments amplifies ^{14}C heterogeneity (higher H^{14}), leading to quasi-linear ^{14}C-grain size relationships. In shallower coastal waters, sediment resuspension processes lead to relatively lower overall H^{14}, but with maximum ^{14}C ages occurring at intermediate grain sizes as a consequence of the propensity of the sortable silt fraction to remobilization and redistribution. The H^{14} parameter may also prove of use as a means to detect the influence of hydrodynamic processes in other (deeper ocean) settings.

The influence of hydrodynamic processes in sedimentary OC ^{14}C contents is common in the CMS, regardless of carbon sources. Indeed, ^{14}C aging of OM as a consequence of this suite of processes is likely prevalent globally, adding a temporal dimension to dispersal of sediments on continental shelves. Due to unique hydrodynamic regimes of each shelf system, the mode and extent of influence will vary, with resulting differences on the fate of OC residing in different grain size fractions. Consequently, events/factors influencing grain size transport and sorting (e.g., sea level change, gravity flows, ocean topography) should be considered to further our understanding of the content and isotopic composition of OC in marine sediments. Hydrodynamically-induced variations in ^{14}C heterogeneity carry implications for our understanding of global OC cycling and its fate on continental margins (Fig. 6). Further studies examining ^{14}C heterogeneity within different OM pools in the context of OM source (e.g., via specific biomarker compounds), or reactivity (e.g., as a function of thermal or biological lability) are warranted.

Acknowledgements

This study was supported by SNF "CAPS-LOCK" project 200021_140850 (T.I.E.), by the National Natural Science Foundation of China (Grant No. 41520104009 and No. U1706219, M.Z.) and by "111" project (B13030). We greatly appreciate the assistance from members of the Laboratory for Ion Beam Physics in all aspects of the AMS measurements. We thank the two anonymous reviewers for their careful reading of our manuscript and their many insightful comments.

Appendix A. Supplementary material

Supplementary material related to this article can be found online at https://doi.org/10.1016/j.epsl.2018.10.013.

References

Aller, R.C., Blair, N.E., 2006. Carbon remineralization in the Amazon–Guianas tropical mobile mudbelt: a sedimentary incinerator. Cont. Shelf Res. 26, 2241–2259.
Arnarson, T.S., Keil, R.G., 2007. Changes in organic matter–mineral interactions for marine sediments with varying oxygen exposure times. Geochim. Cosmochim. Acta 71, 3545–3556.
Bao, R., McIntyre, C., Zhao, M., Zhu, C., Kao, S.-J., Eglinton, T.I., 2016. Widespread dispersal and aging of organic carbon in shallow marginal seas. Geology 44, 791–794.
Bao, R., McNichol, A., McIntyre, C., Xu, L., Eglinton, T.I., 2018. Dimensions of radiocarbon variability within sedimentary organic matter. Radiocarbon 60, 775–790.
Blair, N.E., Aller, R.C., 2012. The fate of terrestrial organic carbon in the marine environment. Annu. Rev. Mar. Sci. 4, 401–423.
Bröder, L., Tesi, T., Andersson, A., Semiletov, I., Gustafsson, Ö., 2018. Bounding cross-shelf transport time and degradation in Siberian-Arctic land–ocean carbon transfer. Nat. Commun. 9, 806.

Chen, C.-T.A., 2009. Chemical and physical fronts in the Bohai, Yellow and East China seas. J. Mar. Syst. 78, 394–410.
Deng, B., Wu, H., Yang, S., Zhang, J., 2017. Longshore suspended sediment transport and its implications for submarine erosion off the Yangtze River Estuary. Estuar. Coast. Shelf Sci. 190, 1–10.
France, R., 1995. Carbon-13 enrichment in benthic compared to planktonic algae: foodweb implications. Mar. Ecol. Prog. Ser., 307–312.
Fu, D., Huang, Z., Zhang, Y., Pan, D., Ding, Y., Liu, D., Zhang, Y., Mao, Z., Chen, J., 2015. Factors affecting spring bloom in the South of Cheju Island in the East China Sea. Acta Oceanol. Sin. 34, 51–55.
Gao, S., Collins, M., 2014. Holocene sedimentary systems on continental shelves. Mar. Geol. 352, 268–294.
Goñi, M.A., Yunker, M.B., Macdonald, R.W., Eglinton, T.I., 2005. The supply and preservation of ancient and modern components of organic carbon in the Canadian Beaufort Shelf of the Arctic Ocean. Mar. Chem. 93, 53–73.
Griffith, D.R., Martin, W.R., Eglinton, T.I., 2010. The radiocarbon age of organic carbon in marine surface sediments. Geochim. Cosmochim. Acta 74, 6788–6800.
Harris, C.K., Wiberg, P., 2002. Across-shelf sediment transport: interactions between suspended sediment and bed sediment. J. Geophys. Res., Oceans 107 (C1), 8–1–8-12.
Hilton, R.G., Galy, A., Hovius, N., Horng, M.-J., Chen, H., 2010. The isotopic composition of particulate organic carbon in mountain rivers of Taiwan. Geochim. Cosmochim. Acta 74, 3164–3181.
Inthorn, M., Mohrholz, V., Zabel, M., 2006. Nepheloid layer distribution in the Benguela upwelling area offshore Namibia. Deep-Sea Res., Part 1, Oceanogr. Res. Pap. 53, 1423–1438.
Jahnke, R.A., Nelson, J.R., Marinelli, R.L., Eckman, J.E., 2000. Benthic flux of biogenic elements on the Southeastern US continental shelf: influence of pore water advective transport and benthic microalgae. Cont. Shelf Res. 20, 109–127.
Kao, S., Hilton, R., Selvaraj, K., Dai, M., Zehetner, F., Huang, J., Hsu, S., Sparkes, R., Liu, J., Lee, T., 2014. Preservation of terrestrial organic carbon in marine sediments offshore Taiwan: mountain building and atmospheric carbon dioxide sequestration. Earth Surf. Dyn. 2, 127–139.
Keller, G.H., Yincan, Y., 1985. Geotechnical properties of surface and near-surface deposits in the East China Sea. Cont. Shelf Res. 4, 159–174.
Komada, T., Anderson, M.R., Dorfmeier, C.L., 2008. Carbonate removal from coastal sediments for the determination of organic carbon and its isotopic signatures, $\delta^{13}C$ and $\Delta^{14}C$: comparison of fumigation and direct acidification by hydrochloric acid. Limnol. Oceanogr., Methods 6, 254–262.
Li, G., Qiao, L., Dong, P., Ma, Y., Xu, J., Liu, S., Liu, Y., Li, J., Li, P., Ding, D., 2016. Hydrodynamic condition and suspended sediment diffusion in the Yellow Sea and East China Sea. J. Geophys. Res., Oceans 121, 6204–6222.
Liu, Z.X., Xia, D.X., Berne, S., Wang, K.Y., Marsset, T., Tang, Y.X., Bourillet, J.F., 1998. Tidal deposition systems of China's continental shelf, with special reference to the eastern Bohai Sea. Mar. Geol. 145, 225–253.
Liu, J., Li, A., Xu, K., Velozzi, D., Yang, Z., Milliman, J., DeMaster, D., 2006. Sedimentary features of the Yangtze River-derived along-shelf clinoform deposit in the East China Sea. Cont. Shelf Res. 26, 2141–2156.
Liu, J., Liu, C., Xu, K., Milliman, J., Chiu, J., Kao, S., Lin, S., 2008. Flux and fate of small mountainous rivers derived sediments into the Taiwan Strait. Mar. Geol. 256, 65–76.
McCave, I., Hall, I.R., 2006. Size sorting in marine muds: processes, pitfalls, and prospects for paleoflow-speed proxies. Geochem. Geophys. Geosyst. 7. https://doi.org/10.1029/2006GC001284.
Megens, L., Van der Plicht, J., De Leeuw, J., Smedes, F., 2002. Stable carbon and radiocarbon isotope compositions of particle size fractions to determine origins of sedimentary organic matter in an estuary. Org. Geochem. 33, 945–952.
McKee, B., Aller, R., Allison, M., Bianchi, T., Kineke, G., 2004. Transport and transformation of dissolved and particulate materials on continental margins influenced by major rivers: benthic boundary layer and seabed processes. Cont. Shelf Res. 24, 899–926.
Milliman, J.D., Beardsley, R.C., Zuo-Sheng, Y., Limeburner, R., 1985. Modern Huanghe-derived muds on the outer shelf of the East China Sea: identification and potential transport mechanisms. Cont. Shelf Res. 4, 175–188.
Mollenhauer, G., Eglinton, T.I., 2007. Diagenetic and sedimentological controls on the composition of organic matter preserved in California Borderland Basin sediments. Limnol. Oceanogr. 52, 558–576.
Mollenhauer, G., McManus, J.F., Wagner, T., McCave, I.N., Eglinton, T.I., 2011. Radiocarbon and ^{230}Th data reveal rapid redistribution and temporal changes in sediment focussing at a North Atlantic drift. Earth Planet. Sci. Lett. 301, 373–381.
Pearson, A., Eglinton, T.I., 2000. The origin of n-alkanes in Santa Monica Basin surface sediment: a model based on compound-specific $\Delta^{14}C$ and $\delta^{13}C$ data. Org. Geochem. 31, 1103–1116.
Qiao, S., Shi, X., Wang, G., Zhou, L., Hu, B., Hu, L., Yang, G., Liu, Y., Yao, Z., Liu, S., 2017. Sediment accumulation and budget in the Bohai Sea, Yellow Sea and East China Sea. Mar. Geol. 390, 270–281.
Ruff, M., Wacker, L., Gäggeler, H., Suter, M., Synal, H.-A., Szidat, S., 2007. A gas ion source for radiocarbon measurements at 200 kV. Radiocarbon 49, 307–314.
Shi, W., Wang, M., 2012. Satellite views of the Bohai Sea, Yellow Sea and East China Sea. Prog. Oceanogr. 104, 30–45.
Sternberg, R., Larsen, L., Miao, Y., 1985. Tidally driven sediment transport on the East China Sea continental shelf. Cont. Shelf Res. 4, 105–120.
Su, C.-C., Huh, C.-A., 2002. ^{210}Pb, ^{137}Cs and $^{239,240}Pu$ in East China Sea sediments: sources, pathways and budgets of sediments and radionuclides. Mar. Geol. 183, 163–178.
Synal, H.-A., Stocker, M., Suter, M., 2007. MICADAS: a new compact radiocarbon AMS system. Nucl. Instrum. Methods Phys. Res., Sect. B 259, 7–13.
Tao, S., Eglinton, T.I., Montluçon, D.B., McIntyre, C., Zhao, M., 2015. Pre-aged soil organic carbon as a major component of the Yellow River suspended load: regional significance and global relevance. Earth Planet. Sci. Lett. 414, 77–86.
Thomsen, L., Gust, G., 2000. Sediment erosion thresholds and characteristics of resuspended aggregates on the western European continental margin. Deep-Sea Res., Part 1 47, 1881–1897.
Thomson, J., Cook, G., Anderson, R., Mackenzie, A., Harkness, D., McCave, I., 1995. Radiocarbon age offsets in different-sized carbonate components of deep-sea sediments. Radiocarbon 37, 91–101.
Thomsen, L., Van Weering, T.C., 1998. Spatial and temporal variability of particulate matter in the benthic boundary layer at the NW European Continental Margin (Goban Spur). Prog. Oceanogr. 42, 61–76.
Tsunogai, S., Watanabe, S., Sato, T., 1999. Is there a "continental shelf pump" for the absorption of atmospheric CO_2? Tellus B 51, 701–712.
van der Voort, T.S., Mannu, U., Blattmann, T.M., Bao, R., Zhao, M., Eglinton, T.I., 2018. Deconvolving the fate of carbon in coastal sediments. Geophys. Res. Lett. https://doi.org/10.1029/2018GL077009.
Wacker, L., Němec, M., Bourquin, J., 2010. A revolutionary graphitisation system: fully automated, compact and simple. Nucl. Instrum. Methods Phys. Res., Sect. B 268, 931–934.
Wang, H., Wang, A., Bi, N., Zeng, X., Xiao, H., 2014. Seasonal distribution of suspended sediment in the Bohai Sea, China. Cont. Shelf Res. 90, 17–32.
Wang, J., Yao, P., Bianchi, T.S., Li, D., Zhao, B., Cui, X., Pan, H., Zhang, T., Yu, Z., 2015. The effect of particle density on the sources, distribution, and degradation of sedimentary organic carbon in the Changjiang Estuary and adjacent shelf. Chem. Geol. 402, 52–67.
Wang, J., Du, J., Baskaran, M., Zhang, J., 2016a. Mobile mud dynamics in the East China Sea elucidated using ^{210}Pb, ^{137}Cs, ^{7}Be, and ^{234}Th as tracers. J. Geophys. Res., Oceans 121, 224–239.
Wang, X., Luo, C., Ge, T., Xu, C., Xue, Y., 2016b. Controls on the sources and cycling of dissolved inorganic carbon in the Changjiang and Huanghe River estuaries, China: ^{14}C and ^{13}C studies. Limnol. Oceanogr. 61, 1358–1374.
Wang, X., Ma, H., Li, R., Song, Z., Wu, J., 2012. Seasonal fluxes and source variation of organic carbon transported by two major Chinese Rivers: the Yellow River and Changjiang (Yangtze) River. Glob. Biogeochem. Cycles 26. https://doi.org/10.1029/2011GB004130.
Wu, P., Bi, R., Duan, S., Jin, H., Chen, J., Hao, Q., Cai, Y., Mao, X., Zhao, M., 2016. Spatiotemporal variations of phytoplankton in the East China Sea and the Yellow Sea revealed by lipid biomarkers. J. Geophys. Res., Biogeosci. 121, 109–125.
Xing, F., Wang, Y.P., Wang, H.V., 2012. Tidal hydrodynamics and fine-grained sediment transport on the radial sand ridge system in the southern Yellow Sea. Mar. Geol. 291, 192–210.
Xu, K., Milliman, J.D., Li, A., Liu, J.P., Kao, S.-J., Wan, S., 2009. Yangtze- and Taiwan-derived sediments on the inner shelf of East China Sea. Cont. Shelf Res. 29, 2240–2256.
Yang, S.Y., Xu, K.H., Milliman, J.D., Yang, H.F., Wu, C.S., 2015. Decline of Yangtze River water and sediment discharge: impact from natural and anthropogenic changes. Sci. Rep.-UK 5. https://doi.org/10.1038/srep12581.
Yang, Z., Liu, J., 2007. A unique Yellow River-derived distal subaqueous delta in the Yellow Sea. Mar. Geol. 240, 169–176.
Yang, Z., Lei, K., Guo, Z., Wang, H., 2007. Effect of a winter storm on sediment transport and resuspension in the distal mud area, the East China Sea. J. Coast. Res., 310–318.
Yang, Z., Ji, Y., Bi, N., Lei, K., Wang, H., 2011. Sediment transport off the Huanghe (Yellow River) delta and in the adjacent Bohai Sea in winter and seasonal comparison. Estuar. Coast. Shelf Res. 93, 173–181.
Zeng, X., He, R., Xue, Z., Wang, H., Wang, Y., Yao, Z., Guan, W., Warrillow, J., 2015. River-derived sediment suspension and transport in the Bohai, Yellow, and East China Seas: a preliminary modeling study. Cont. Shelf Res. 111, 112–125.
Zhou, C., Dong, P., Li, G., 2015. Hydrodynamic processes and their impacts on the mud deposit in the Southern Yellow Sea. Mar. Geol. 360, 1–16.
Zhu, Y., Chang, R., 2000. Preliminary study of the dynamic origin of the distribution pattern of bottom sediments on the continental shelves of the Bohai Sea, Yellow Sea and East China Sea. Estuar. Coast. Shelf Res. 51, 663–680.
Zhu, Z.Y., Zhang, J., Wu, Y., Lin, J., 2006. Bulk particulate organic carbon in the East China Sea: tidal influence and bottom transport. Prog. Oceanogr. 69, 37–60.